Advanced characterization of two novel Fe-rich high entropy alloys developed for laser powder bed fusion in the Al-Co-Cr-Fe-Ni-Zr system

M.S. Knieps [a,b], O.M.D.M. Messé[a], P. Barriobero-Vila [c,d], U. Hecht [e]

[a] Oerlikon AM Europe GmbH, Kapellenstraße 12, Feldkirchen 85622, Germany

[b] Faculty of Georesources and Materials Engineering, RWTH Aachen University, Germany

[c] Institute of Materials Research, German Aerospace Center (DLR), Linder Höhe, Cologne 51147, Germany

[d] Department of Materials Science and Engineering, Technical University of Catalonia (UPC), Eduard Maristany Av. 16, Barcelona 08019, Spain

[e] Access e.V., Inztestr. 5, Aachen 52072, Germany

Abstract

Laser powder bed fusion (LPBF) was used to manufacture two high entropy alloys (HEAs) within the Al-Co-CrFe-Ni-Zr system. The selected compositional ranges were similar to alumina forming austenitic (AFA) steels but omitting interstitials and replacing Nb with Zr as the Laves forming element. The Fe-rich austenitic HEAs were prepared with varying Al and Zr content to evaluate the influence on the presence, size, and distribution of the intermetallic (IM) precipitates. The LPBF process combined with a single (950 °C 6 h) heat treatment formed large, elongated grains with a fine dispersion of multiple different nano-sized IM phases. Synchrotron high energy x-ray diffraction (HEXRD) revealed the cubic $M_{23}Zr_6$ as the main Zr-rich IM phase, stabilized by the multi-element mixture (M=Co, Fe, Ni) and the high cooling rates of the LPBF process. Further HEXRD *in-situ* compression was performed from room temperature to 900 °C to evaluate the phase stability, thermal expansion, and the strength contribution of the austenitic matrix and the $M_{23}Zr_6$ and NiAl

B2 IM phases. The evolution of lattice strain and full width at half maximum of the reflexes was tracked using a statistical model, enabling quantitative analysis along the deformation.

Introduction

Iron-based austenitic materials are widely used in high temperature applications such as super-heaters and turbine components for power plants or manifolds and turbochargers for automotive engines [1,2]. Heat resistant austenitic steels are characterized by good strength at elevated temperatures, resistance to creep, oxidation, and corrosion, and are more cost-effective than Nickel-based alloys. However, sustainability and the economic trends push for higher power densities and efficiencies, resulting in more demanding performance requirements. Therefore, increased operating temperatures and more corrosive environments have driven the development of heat resistant austenites for several years, yielding continuously evolving concepts [3–6].

The strengthening through fine precipitates like carbides and intermetallics (IM), such as Fe_2M type Laves-phases, is a well proven approach for iron-based heat resistant austenites. The addition of aluminum improves the oxidation resistance by forming a stable Al_2O_3 protective layer [7–10]. Alloys combining these two approaches are known as alumina-forming austenitic (AFA) steels and have compositions with wt.% ranges of Fe (42–72), Ni (12–35), Cr (12-19), Al (2.5–4), Nb (0.6–3) together with minor additions of C, Ti, Si, or B [11–13]. These highly alloyed steels provide precipitation strengthening from multiple phases like B2, γ' and Laves [13]. Li et al. reported a $(FeCoNi)_{81}Cr_9Al_8Ti_1Nb_1$ high entropy alloy (HEA) using a similar alloy design concept which provided outstanding high temperature performance [14]. Generally, the field of HEAs with the multi-principal element approach opens new possibilities to improve high temperature properties [15,16]. Nevertheless, to maintain the economic attractiveness of the current heat resistant austenites like AFA steels, the novel

alloying concepts should limit the fractions of expensive elements such as Co, Ni or refractories and keep an Fe-rich baseline.

Fe_2Nb is the Laves phase commonly used in AFA steels but Zr is lighter and cheaper than Nb and also forms Laves IMs stable up to the melting point in equilibrium with an austenitic Fe-rich or HEA matrix [7,17]. Multiple studies have explored the solubility and stability of Zr containing IMs in Fe or Ni-rich HEA systems and reported outstanding oxidation resistance of the Al and Zr combination [18–21]. Furthermore, Fe_2Zr reinforced materials (ferritic and austenitic) have demonstrated good high temperature strength and creep performance [22–26]. For high temperature strength and good creep performance, typically a microstructure of large grains with a fine dispersion of stable IM phases of sub-micron size is beneficial. Fewer grain boundaries reduces the effect of grain boundary sliding and the small precipitates restrain the intragranular dislocation movement [27,28]. To achieve such a microstructure, heat resistant austenites are typically solutionized at 1050-1250 °C to homogenously distribute all solute elements then aged around 750 °C to generate the precipitates of desired size. This is often combined with mechanical treatments such as hot or cold rolling to adjust the grain size [3,8–11].

An alternative way of achieving the fine dispersion of IMs in relatively large grains is through additive manufacturing (AM) and the associated directional and fast cooling. Metal AM processes enable the production of complex geometries and components in comparably short lead times and have become attractive alternatives to conventional manufacturing. Among the metal AM techniques, laser powder bed fusion (LPBF) offers the highest cooling rates ranging from 10^5 to 10^6 K/s [29]. The thermal conditions in LPBF melt pools produce a non-equilibrium solidification resulting in a cellular growth morphology of the austenite within large columnar grains. The cellular spacing and the associated micro-segregation pattern are commonly in the submicrometer range [30–32]. Eventually, nano-scale IM phases from in the intercellular regions during the final stages of solidification.

This as-solidified microstructure requires a suitable heat treatment for stress relief and/or direct aging, to further precipitate IM phases inside the micro-segregated cellular arrays. Thus, along with an adequate heat treatment, LPBF could allow achieving an ultrafine dispersion of IM particles inside the large columnar grains.

Aiming at examining this approach, we propose a new type of IMreinforced austenitic material manufactured by LPBF. Two Fe-rich HEAs from the Al-Co-Cr-Fe-Ni-Zr system have been prepared in composition ranges similar to current AFA steels, excluding the minor additions of interstitials. Additionally, the sum of Co and Ni did not exceed 35 wt.%, and the laves forming element Nb was substituted by Zr. The two HEAs were produced by blended powders of deliberately selected Al and Zr contents, to investigate the influence of composition on the formation of precipitates. After extensive microstructural characterization, the alloys were examined using *in-situ* high-energy synchrotron X-ray diffraction (HEXRD) during compression at selected temperatures from room temperature up to 900 °C. This *in-situ* technique provides a deep and continuous insight to the deformation kinetics, phase stability and the contribution of the different phases to the mechanical performance at high temperatures [33–35]. The results obtained enable an assessment and understanding of this new multiphase HEA approach for heat resistant austenitic materials.

Materials and methods

The alloys used in this study were prepared from powder blends according to nominal composition in at.% in Table 1. Corresponding to the Al and Zr content, the two alloys will be referred as A4Z3 and A9Z2. The blends were prepared by mixing pure elemental Fe, Co, Cr and Ni powders with different prealloyed HEA powders. The used prealloyed HEAs were from the Al-Cr-Fe-Ni and Al-Co-Cr-Fe-Ni-Zr system, with spheri cal shape and a particle size distribution of −45+15 μm. The elemental Fe, Co and Ni powders were spherical fines with a size of <25 μm. The elemental Cr presented angular shape and <45 μm in size. The blend ing was carried out using a stainless-steel double cone vessel rotating at 30 rpm for 2 h. This procedure

has been previously proven to give homogenous elemental HEA blends [36].

The LPBF processing of the alloys was done on a Truprint1000 machine, equipped with a 200 W laser and a spot size of 55 μm. Vertically oriented blocks with dimensions of 10 × 10 × 35 mm were built under Argon on a stainless-steel baseplate using a scan speed of 600 mm/s, laser power of 170 W and 30 μm layer thickness. The utilized scan strategy was a meander line pattern with 80 μm hatch distance and 90° rotation between consecutive layers. After processing, the blocks were removed from the baseplate via electro discharge machining. One block from each alloy was kept in the as-built condition. The other blocks were heat treated at 950 °C for 6 h in Argon atmosphere. Metallographic sections were prepared along the build direction, longitudinal section (LS), and perpendicular to the build direction, cross section (CS), for both the as-built and heat-treated condition. The samples were mechanically polished down to 0.25 μm with colloidal silica suspension and imaged with a Zeiss Smartzoom digital microscope for porosity analysis. For microstructure visualization and characterization, a Zeiss Merlin SEM equipped with Oxford Instruments X-MaxN EDS and NordlysNano EBSD detectors was used. Image analysis was performed on 5000x magnification SEM micrographs of the heat-treated CS samples to characterize the area fraction of the different precipitates as well as their major and minor ellipsis axis (E.A). To quantify the distribution of the precipitates, the distance between neighboring particles (δ) was measured using Delaunay triangulation [37,38]. All image analysis was caried out using the software ImageJ [39]. Additionally, HV1 hardness measurements were performed on both alloys in the as-built and the heat-treated condition using a Struers DuraScan microhardness testing equipment.

For the *in-situ* HEXRD compression samples, heat-treated blocks were machined and cut into cylinders of 3.5 mm diameter and 6.5 mm height. Multiple cylinders were extracted from each block. The *in-situ* HEXRD compression tests were carried out at the beamline P07-HEMS of PETRA III, Deutsches Elektronen-Synchrotron (DESY) [40]. Uniaxial compression was

performed at room temperature (RT), 600 °C, 700 °C, 800 °C and 900 °C using a deformation unit incorporated in a modified dilatometer Bähr 805A/D [33]. The cylinders were deformed along the LPBF build direction at a strain rate of $0.001 \, s^{-1}$. During deformation, the X-ray beam was positioned to the middle of the sample's length and perpendicular to the loading direction. Sequences of entire Debye-Scherrer rings from the bulk samples were recorded in transmission mode during compression using a Perkin Elmer XRD 1621 image-plate detector. A slit size of $0.8 \times 0.8 \, mm^2$ resulting in a gage volume of $0.8 \times 0.8 \times 3.5 \, mm^3$ was used. The sample-detector distance was 1788.4 mm, and the acquisition time 1 s. An illustrative diagram of the experimental setup is presented in [41]. The beam energy was 100 keV, with a wavelength of 0.124 Å. The instrument parameters were calibrated using a LaB_6 powder standard.

Quantitative phase analysis of the entire Debye-Scherrer rings in undeformed state was carried out employing the Rietveld method as implemented in the software Material Analysis Using Diffraction (MAUD). It uses an extended Williams-Imhof-Matthies-Vinel algorithm (E-WIMV) for texture analysis [42].

The lattice strain (εi) of selected {hkl} reflections can be calculated according to Eq. (1), where $d0$ is the initial interplanar lattice spacing and di corresponds to the spacing in the current deformation state i. The reflections were calculated parallel (axial) and perpendicular (radial) to the loading direction, considering integrations of cake portions of 10° Applying the Bragg's law, Eq. (2), on Eq. (1) it yields Eq. (3) from which the lattice strain can be calculated as a function of the θ angle.
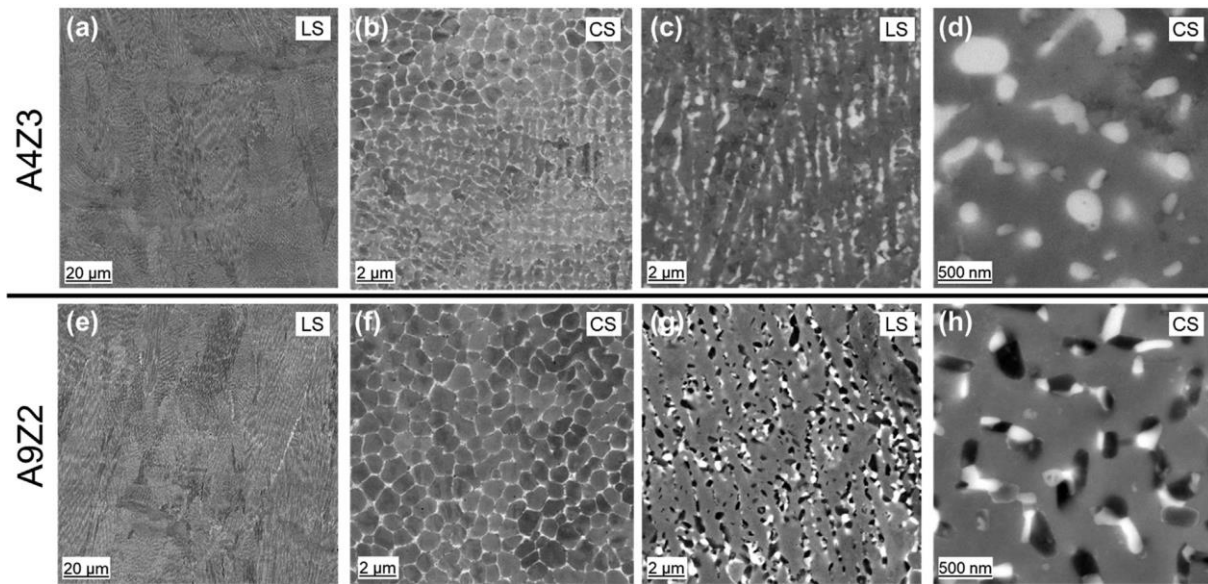
Fig. 1. SEM microstructure images of (a, b) A4Z3 as-built; (c, d) A4Z3 heat-treated; (e, f) A9Z2 as-built; (g, h) A9Z2 heat-treated.

For the analysis of the peaks and the resulting lattice strain during the compression, the axial and radial spectra were fitted using a statistical python model. From the model the position and shape for all the peaks was fitted throughout the whole deformation for both alloys and for all temperatures. Based on Eq. (3), the lattice strain was calculated for the peaks based on their 2θ position. Moreover, the model enabled to track the evolution of the full width at half maximum (FWHM) and the peak height. To verify the model, the lattice strain evolution was also calculated with Eq. (1) using the interplanar spacing obtained from the Rietveld refinement from the MAUD software. This verification was done for the axial direction for the FCC matrix peaks {200} and {220}, and the {333} peak of the Zr-rich cubic $M_{23}Zr_6$ phase for both alloys and 3 temperatures (RT, 600 °C and 900 °C). The verification for A9Z2 additionally included the {200} and {110} of the BCC peaks. For each of the reflexes 10 points got selected at different stages along the compression. 4 Points between 0 and 5% compressive strain and 6 points from 5% up to 30% compressive strain got selected depending on the alloy and temperature. The plot showing the lattice strain of the examined points for the model verification is added in the supplementary material.

Results

Microstructure characterization

The two alloys were LPBF processed as described in the previous section. The parameters yielded material with a density of $99.90 \pm 0.05\%$ for A4Z3 and $99.95 \pm 0.01\%$ for A9Z2. The microstructure in the as-built state as well as after heat treatment is shown in Fig. 1. The micrographs depict the longitudinal section and cross section for the as-built and heat-treated condition for each alloy.

In the as-built state, both alloys exhibit an ultrafine cellular/dendritic microstructure. The heat treatment dissolved the microsegregation and lead to sub-micron sized IM precipitates. EDS maps on the heat-treated samples revealed that the gray matrix is Fe and Cr rich and the bright IMs are rich in Zr. Additionally, the dark precipitates appearing for A9Z2 are rich in Ni and Al, expected to be NiAl B2. The EDS maps are available in the supplementary material.

From EDS maps it was also remarkable that Co appeared to be equally present in the matrix and all IM phases. Additionally, multiple area spectra showed that the overall resulting chemistry for the processed blends was in accordance with the nominal compositions in Table 1. The biggest deviation was found for Co, Cr and Fe with average for both alloys of ±1.34 at.%. For Al, Ni and Zr the average deviation was in the range of ±0.31 at.% for both alloys.

The results of the CS SEM image analysis in terms of area fractions of the bright and dark phases, their major and minor ellipsis axis, as well as the Delaunay distance are displayed in Table 2.

The EBSD analysis revealed that both alloys present an FCC matrix with large grains elongated in the build direction. The heat treatment carried out did not produce a visible change in grain size or texture for the FCC matrix. The Zr-rich IMs could not be imaged unambiguously with the available EBSD and sample preparations setup. It appears that they are comprised of multiple cubic IM phases which would require higher resolution for precise Kikuchi band

pattern differentiation. For this reason, the EBSD analysis was focused on the Matrix and omitted for the different precipitates. Fig. 2 depicts an EBSD map of alloy A9Z2 with the corresponding pole figure and inverse pole figure, showing a predominant cubic texture of the matrix aligned with the build direction (BD).

The results from the hardness measurements of A4Z3 showed a small reduction from the as-built condition (306±15 HV1) to the heat-treated condition (272±5 HV1). In the case of A9Z2, the as-built hardness (308±9 HV1) was not different from the heat-treated state (303±4 HV1).
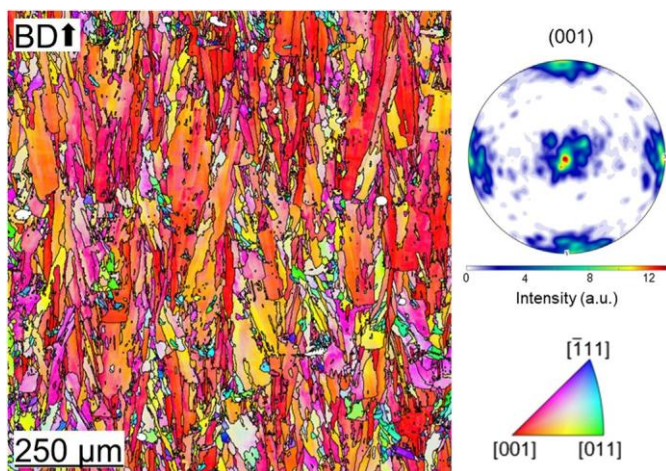

Fig. 2. EBSD micrograph of the A9Z2 alloy in the heat-treated and undeformed state including the pole figure and the invers pole figure in the build direction. For colors, please see digital version.

In-situ HEXRD compression

The HEXRD spectra were analyzed for both alloys for the studied temperatures in the undeformed state i.e., before compression started. The corresponding diffractograms are shown in Fig. 3. Both alloys present 4 clear FCC peaks which belong to the matrix and correspond to the orientations of {111}, {200}, {220} and {311} with increasing 2θ angle. BCC peaks are clearly visible with high intensity in the A9Z2 alloy and are attributed to the Niand Alrich precipitates. Nevertheless, also A4Z3 shows scarce and low intensity traces of the BCC peaks. The 3 marked BCC peaks for the A9Z2 alloy are {110}, {200} and {211} with increasing 2θ

angle. Multiple peaks of medium to low intensity belong to different Zr-rich IMs. The predominant IM phase is the cubic M23Zr6 phase, which is equally present for both alloys and were M can be equivalent to Fe, Ni or Co. The 10 marked M23Zr6 peaks in Fig. 3 correspond to the orientations of {222}, {331}, {420}, {422}, {511}, {333}, {440}, {531}, {731} and {751} with increasing 2θ angle. The other peaks correspond either to cubic Laves M2Zr, monoclinic M7Zr2 or cubic M5Zr, but due to low intensity and potential overlaps no distinct identification was possible and were labeled as MXZrY. The phase identification is addressed in more detail in the discussion section. Due to the multiple different overlaps and remaining unidentified phases, a precise assessment of phase fraction via HEXRD was not possible.

The lattice parameter evolution over the temperatures is shown on the left side in Fig. 4. In the case of the scarce and low intensity BCC peaks for A4Z3, the lattice parameter could not be determined clearly throughout the temperatures. For the same reason, a proper fitting with the statistical model was not possible and the BCC analysis for A4Z3 was omitted.

With the change of lattice parameter (a) over the temperature in difference to RT, the coefficient of thermal expansion (CTE) was estimated with the following Eq. (4) [43,44].
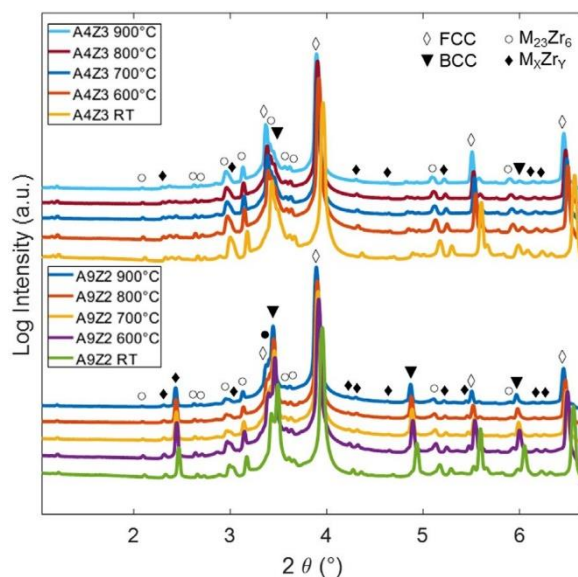
Fig. 3. HEXRD spectra acquired for both alloys at RT and at 600 °C, 700 °C, 800 °C, and 900 °C in the undeformed state. For colors, please see digital version.
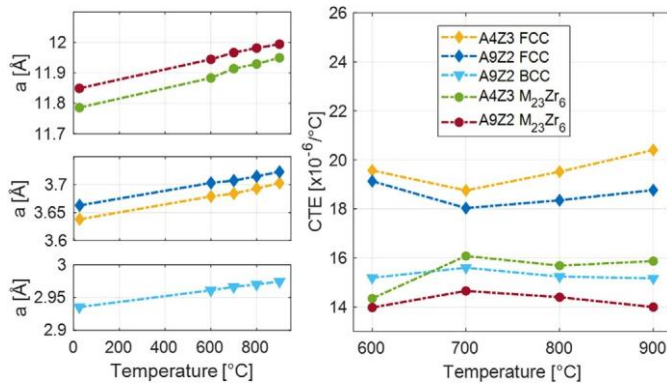

Fig. 4. Left side: lattice parameter evolution from RT to 900 °C for FCC and M23Zr6 for A4Z3 and for FCC, BCC and M23Zr6 for A9Z2. Right side: change of CTE based on the lattice parameter evolution of the different phases and temperatures. For colors, please see digital version.
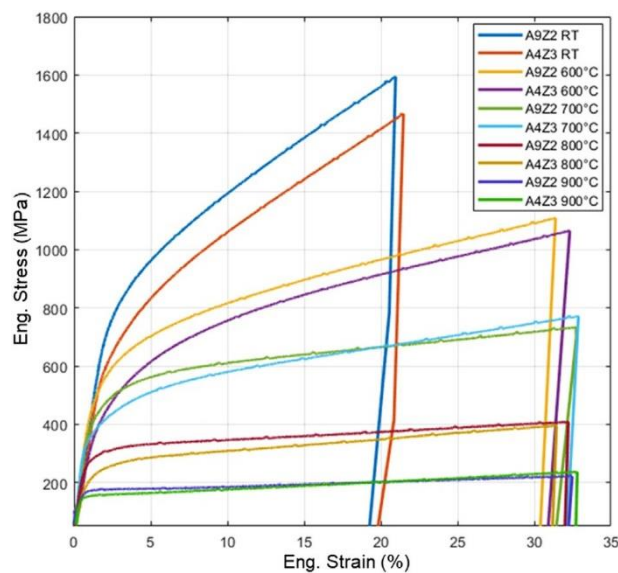

Fig. 5. Engineering stress-strain curves of the *in-situ* HEXRD compression on A4Z3 and A9Z2 for RT, 600 °C, 700 °C, 800 °C, and 900 °C. For colors, please see digital version.
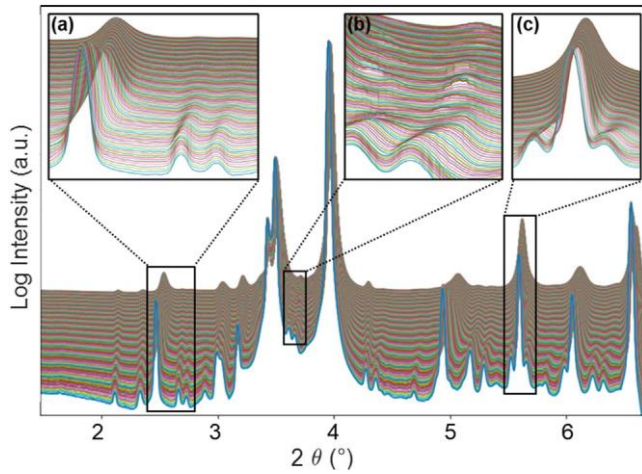
Fig. 6. Waterfall plot of all the diffractograms acquired during the compression of A9Z2 at RT from bottom to top. The enlarged sections show the 2θ ranges of (a) 2.39–2.83°, (b) 3.60–3.75° and (c) 5.45 5.70°.

The engineering stress-strain curves of the in-situ HEXRD compression tests for RT, 600 °C, 700 °C, 800 °C, and 900 °C are shown in Fig. 5. All samples showed a continuous deformation with the compression typical non-uniform change in area (barreling). The barreling increased with higher temperatures but all samples were deformed without buckling or visible crack initiation and were not compressed to failure. RT sample compression was stopped after 20% strain and the high temperature samples after roughly 30%. The small recurrent bumps along the stress-strain curves are a side effect from the hydraulic compression unit and not related to the material behavior. For both alloys the compressive yield strengths for the different testing temperatures are displayed in Table 3.

An example of the evolution of the diffractograms under compressive stress and the resulting deformation is visualized in Fig. 6. It shows all the diffractograms acquired during the compression of A9Z2 at RT plotted from bottom to top with increasing compressive strain from 0 to 20%. The distortion of the lattice resulting from compression led to a peak broadening and position shift towards larger 2θ values. Furthermore, the arising lattice strain diminished the

intensity of the peaks. The logarithmic scale in Fig. 6 leads to an apparent larger drop in intensity with the stacking along the y axis, but it enables a better overview of the peak evolution during the compression than a linear scale. Due to position shifts, some peaks belonging to different phases started overlap ping, hindering unambiguous phase tracking with the statistical model. No phase transformation was observed during compression. This was true for all tested temperatures for both alloys. The enlarged sections from Fig. 6(a)–(c) show examples of the peak shift, broadening and overlapping with ongoing compression. Fig. 6(b) also visualizes abrupt disand re-appearance of small peaks with sudden changes in intensity and position shifts. All these features present in the raw data constitute the main challenges for the continuous data fitting of the statistical model. For this reason, some peaks could not be fitted properly throughout the entire deformation.

A summary of the results of the statistical model for the compression of both alloys at RT is shown in Fig. 7. It depicts the evolution of the lattice strains and of the FWHM for the main FCC, M23 Zr6 and BCC peaks during deformation for the axial and radial direction. Since the compressive load resulted in negative lattice strain values in axial direction and positive values in radial direction, the values for both integrations can be visualized in the same plot in Fig. 7(a) for A4Z3 and (b) for A9Z2. For the FWHM the plots corresponding to the axial and radial integrations are displayed in Fig. 7(c) and (d) for A4Z3 and (e) and (f) for A9Z2, respectively. Outlying or edgy behavior as well as causeless straight lines are indications that the model lost track or misfitted the affected section because of the previous mentioned features which occur during deformation. In most cases the relevant and main intensity peaks were fitted properly throughout the entire deformation for all temperatures. The combined visualization of axial and radial integration enables a good estimation of the results. With higher testing temperature the maximum compressive strain reached is also increased. To keep the visualized range consistent, displaying the elastic range as well as a sufficient portion of the plastic region, the visualization was limited up to 20% compressive strain for all samples and temperatures. The fitted model

results for the evolution of the lattice strain and the FWHM during compression for a selection of phase representative peaks are shown in Fig. 8 and Fig. 9 respectively. Due to the high number of different peaks and the misfitting occurring on some peaks with ongoing deformation, a selection of the main peaks was visualized for interpretation. The representative orientation peaks selected were {200} for FCC, {222} for M23 Zr6 and {200} for BCC. The lattice strain over compressive strain plots in Fig. 8 (a, b) for A4Z3 and (c–e) for A9Z2 combines the axial and radial integration, distinguishable by their negative and positive sign. The plots of the evolution of the FWHM are separated into axial and radial components and displayed in Fig. 9 (a–e) for A4Z3 and (f–j) for A9Z2.

The texture analysis results of the E-WIMV algorithm from MAUD software are displayed in Fig. 10. The algorithm expresses the texture intensity as probability of multiples of random distributions (mrd) of the selected FCC phase reflex. The pole figures shown in Fig. 10 correspond to the {200} plane sets normal to the building and loading direction. The texture results of the undeformed state based on the volume information from the synchrotron data correlate well with the EBSD results of the cubic texture for the FCC matrix (Fig. 2). The pole figures of the compressed conditions correspond to the Debye-Scherrer rings acquired at 20% compressive strain. All the compressed samples, regardless of the testing temperature, presented almost no change in texture compared to the undeformed state. For A4Z3 a loss of texture sharpening is visible for deformation at higher temperatures, as compared to A4Z9.
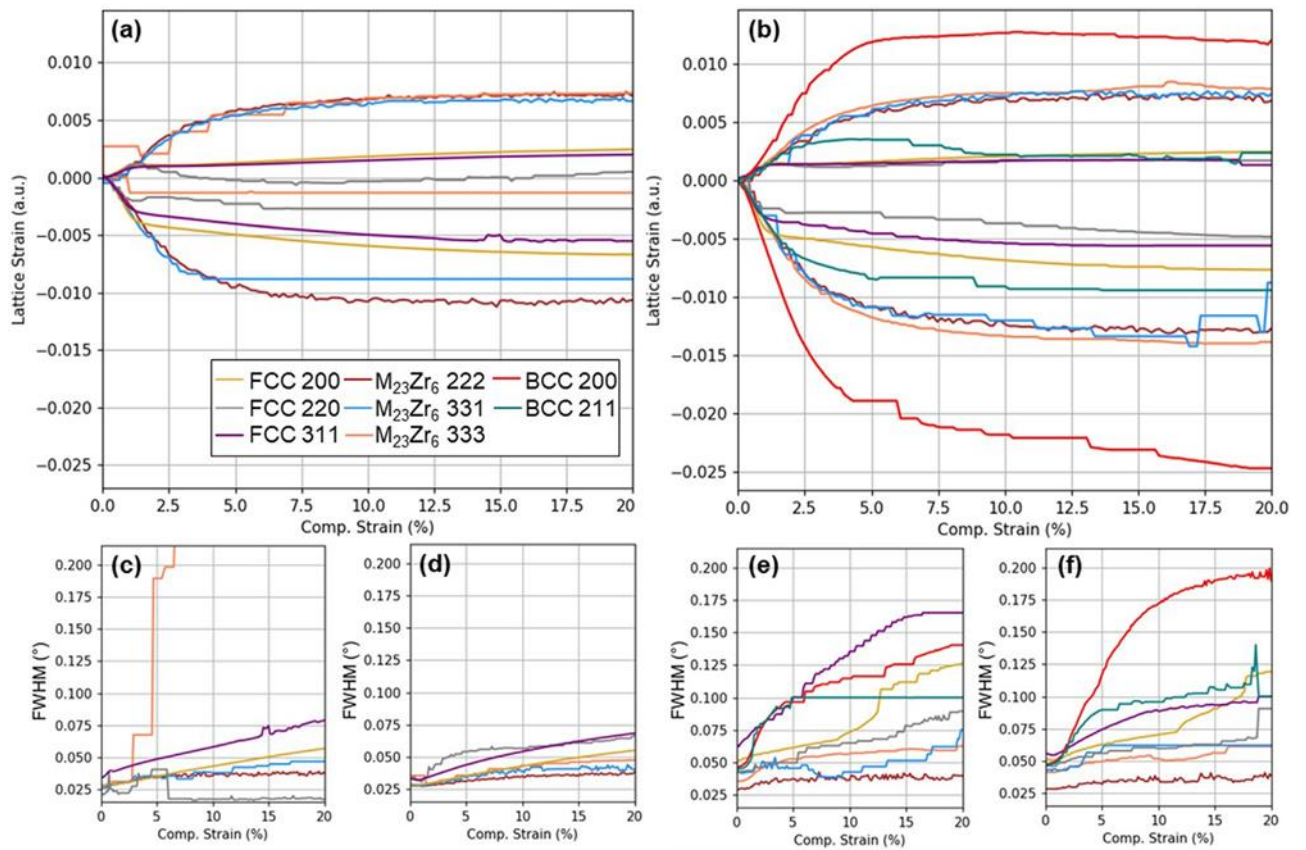
Fig. 7. Statistical model results for the main FCC, M23Zr6 and BCC peaks for both alloys compressed at RT, showing the evolution of the lattice strain of the axial and radial integration for A4Z3 (a) and A9Z2 (b); the evolution of the FWHM for A4Z3 axial (c), A4Z3 radial (d), A9Z2 axial (e), and A9Z2 radial (f). The results indicate signs of misfit and loss of track of the model for: A4Z3 FCC 220 axial and radial, M23Zr6 331 axial and 333 axial, and for A9Z2 BCC 211 axial. For colors, please see digital version.

Discussion

Alloy concept

The presented HEAs within the Al-Co-Cr-Fe-Ni-Zr system, A4Z3 and A9Z2, have Fe as main and low-price matrix constituent, and were prepared with deliberately selected Al and Zr contents. The compositions (Table 1) were set to obtain materials with distinct precipitate fractions (Table 2) in order to evaluate their influence on the materials properties.

The compositional range of the presented HEAs has similarities to AFA steels but using Zr as Laves-phase forming element (instead of Nb), and free of C or other interstitial additions. In such austenitic materials, the main contribution of Al is the formation of the stable protective oxide layer and the stabilization of BCC phases such as NiAl B2, which add strength and act as Al reservoirs for the oxide formation [6]. AFA Steels matrixes have typically Al solubilities ≤ 2 wt.%. Further Al would lead to B2 formation together with Ni [9]. Besides promoting Al oxide layer formation, higher Al content also reduces the alloys density. Greater than 9% at.% Al in Al_X CoCrFeNi HEAs have been reported to stabilize the BCC preferentially to the FCC matrix [45]. Therefore, to explore the Al solubility ranges while maintaining an FCC austenitic matrix, the span of the presented alloys was set to 4–9 at.% Al (1.9–4.3 wt.%).

The selected Zr contents from 2 to 3 at.% (3.3–4.9 wt.%) are above the average range when compared to the Nb values of 0.5–2 at.% (1– 3.3 wt.%) from typical AFA steels or related HEAs [9,14,46]. The examined relatively high Zr contents were set aiming for increased strength through higher fractions of strength attributing Zr-rich IMs and to compensate the absence of carbides, which have a major contribution to the high temperature strength and creep resistance in AFA steels [5]. Further increasing Zr would be less cost effective and could lead to eutectic solidification in the interdendritic region yielding a different microstructure than targeted with the here presented LPBF approach [25].

Apart from the variation in Al and Zr content, both alloys have relatively high Cr and Ni contents and additionally 10–15 at.% Co to fit the HEA concept. Cr is known to improve oxidation resistance and can aid the formation of a protective Al_2O_3 layer through the so called third element effect [9,47]. High Ni content is also known to improve heat and oxidation resistance. Especially the combination of Ni with Al and Zr containing IMs has been reported with outstanding oxidation resistance for ternary Ni-Al-Zr alloys [20,21]. It is fair to expect a good oxidation resistance of the presented HEAs, yet the examination is to be performed as part of future work.

Microstructural features and morphology

The LPBF processing of A4Z3 and A9Z2 yielded the cellular/dendritic structures and elongated grains expected from literature [30,31]. Furthermore, the single heat treatment led to the expected homogenous and fine distribution of nano-sized precipitates while keeping the elongated grain structure (Figs. 1 and 2). The as-built sub-micron cells and dendrites were composed of the FCC matrix with the Zr rich IMs as the fine cell rims and in the interdendritic regions. The single step heat treatment stress relieved the alloys and dissipated the cellular structure while keeping the fine distribution. Furthermore, the heat treatment led to the precipitation of NiAl B2 from the Al oversaturated FCC matrix of A9Z2. The chosen temperature (950 °C) was higher than typical stress relief or aging temperatures of related austenitic steel concepts (600-750 °C) [31,48]. The higher temperature presumably accelerated the phase growth, diminishing the archived refinement, but was important to assure sufficient phase stability during operation when aiming for service temperatures >750 °C [49].

To compare the achieved precipitate fractions and size distributions obtained along the LPBF process route to conventional processing, the data from Table 2 was summarized and plotted together with data for different AFA steels from literature in Fig. 11. Please note that the Nb/Zr IM refers to the Nb containing Laves phase (in the case of the AFA steels), and to different Zr-rich phases, mainly $M_{23}Zr_6$, Laves and other for the presented HEAs. For a better overview of the influence of the Al and Nb/Zr content on the precipitates, the AFA steels have been named following the same scheme as the HEAs: AXNY, were X and Y correspond to the A=Al and N=Nb content in at.%, respectively.

As Fig. 11 depicts, the fraction of the IM phases achieved in A9Z2 is comparable to AFA steels, while A4Z3 stands out through the absence of NiAl B2. Furthermore, the resulting sizes of precipitates in A9Z2 and A4Z3 is comparable, and only slightly higher than in Al8N1. It is worth noting that A8N1 refers to processing through multiple forging, hot and cold rolling steps followed by aging at 700 °C [48]. As previously stated, the higher temperatures for aging

i.e. 950 °C applied in this work, promoted more pronounced coarsening. Other differences certainly relate to phase equilibria being different in the HEAs compared to AFA steels: In both HEA alloys the $M_{23}Zr_6$ and other M_xZr_y IM phases seem to be more stable than the Laves phase M_2Zr, while Fe_2Nb is the prominent phase in the AFA steels.

The interparticle distance between the Zr-rich IM particles was around 770 nm and 670 nm for A4Z3 and A9Z2 respectively, and around 700 nm for the NiAl B2 of A9Z4 (Table 2). For comparison the interparticle distance in A8N1 AFA steel was calculated following the work from Gao et al. [48]. The Delaunay distances between strengthening precipitates (Fe_2Nb and NiAl B2) for this extensively processed AFA steel were found to be 480–640 nm, depending on the amount of deformation implemented during cold rolling [48]. The comparison shows that LPBF processing and direct aging can lead to very fine dispersion of the IM particles, above those reported in literature for AFAs or related HEAs. As before, the high temperature of 950 °C selected for aging may be the prime reason along with the associated coarsening.
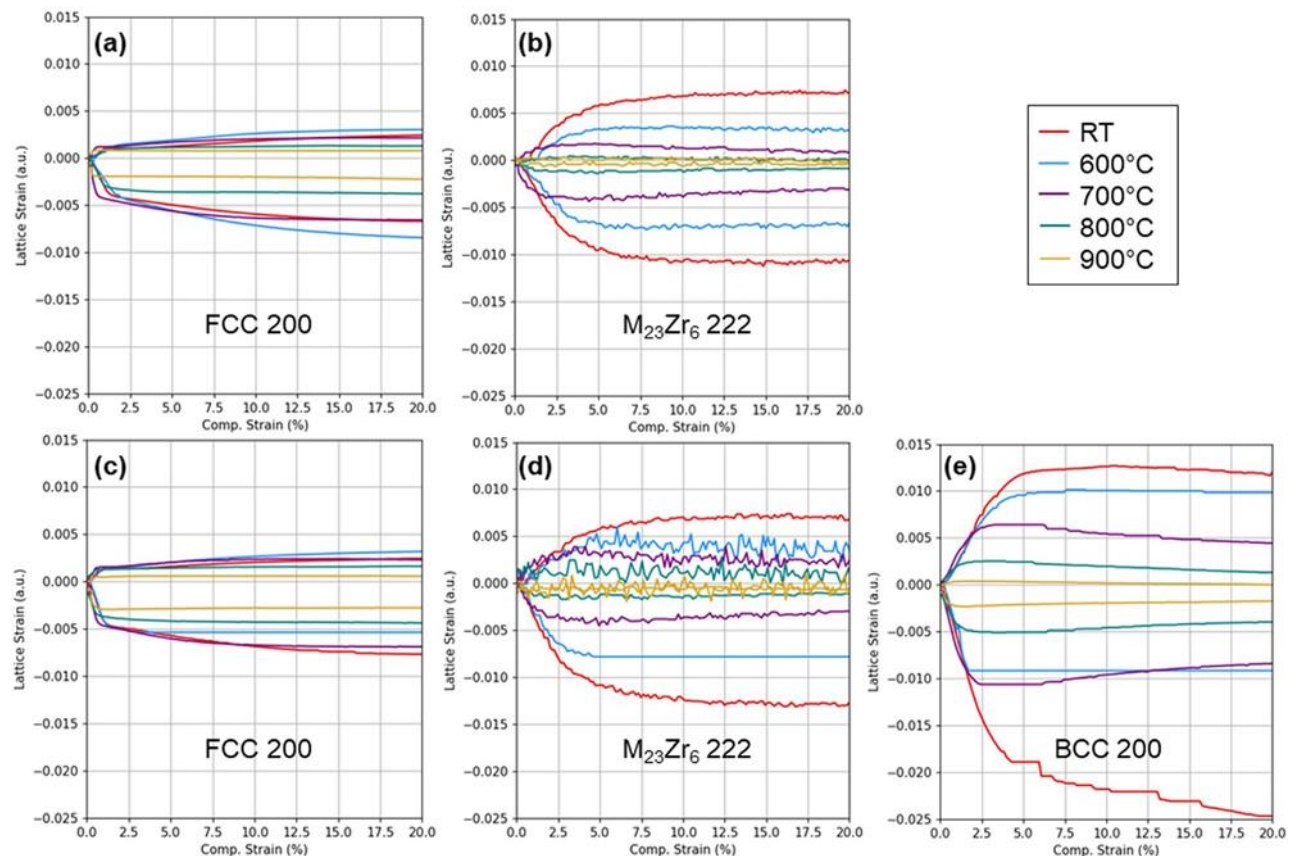
Fig. 8. Model results for the lattice strain evolution of FCC 200, $M_{23}Zr_6$ 222 and BCC 200 during compression at RT, 600 °C, 700 °C, 800 °C and 900 °C of A4Z3 (a, b) and A9Z2 (c–e). The results indicate signs of misfit and loss of track of the model for the axial curves for FCC 200, $M_{23}Zr_6$ 222 and BCC 200 at 600 °C for A9Z2. For colors, please see digital version.
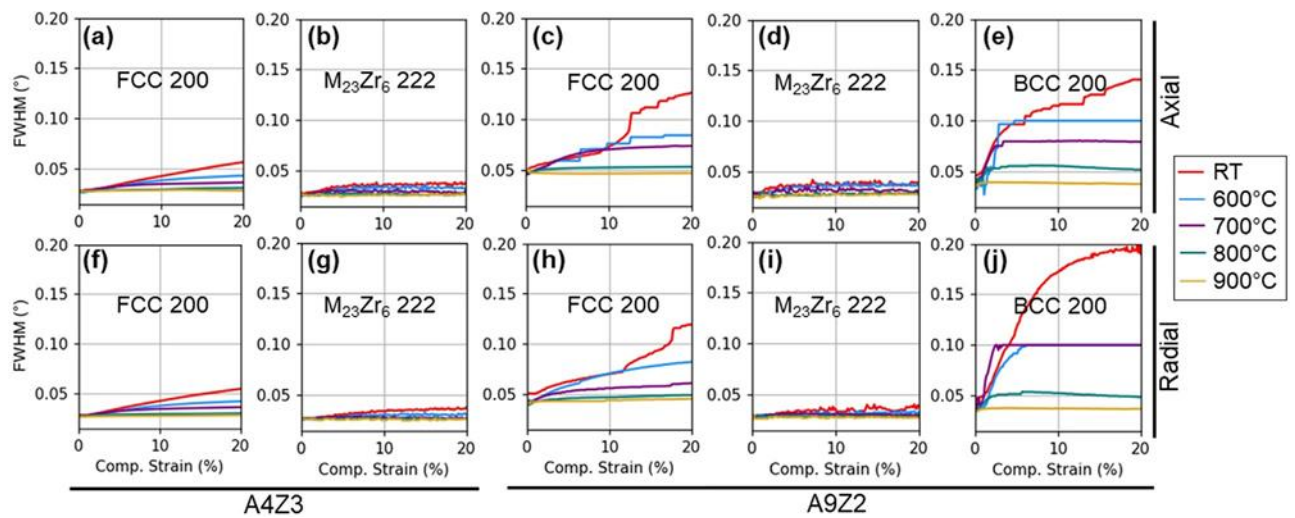

Fig. 9. Model results for the FWHM evolution of FCC 200, $M_{23}Zr_6$ 222 and BCC 200 peaks during compression at RT, 600 °C, 700 °C, 800 °C, and 900 °C of A4Z3 axial (a, b), A9Z2 axial (c–e), A4Z3 radial (f–g) and A9Z2 radial (h–j). The results indicate signs of misfit and loss of track of the model for the axial and radial curves for A9Z2 BCC 200 at 600 °C and 700 °C. For colors, please see digital version.
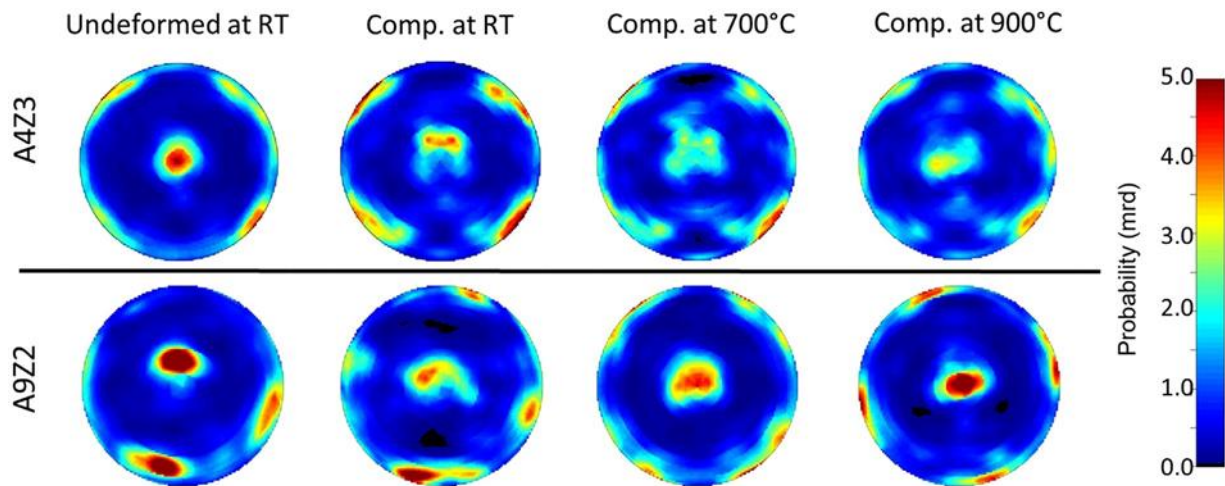
Fig. 10. E-WIMV algorithm texture results of the {200} FCC peak for the undeformed sate and RT and deformed 20% comp. strain at RT, 700 °C, and 900 °C for A4Z3 (top row) and A9Z2 (bottom row). Building and loading direction are normal to the pole figures. For colors, please see digital version.
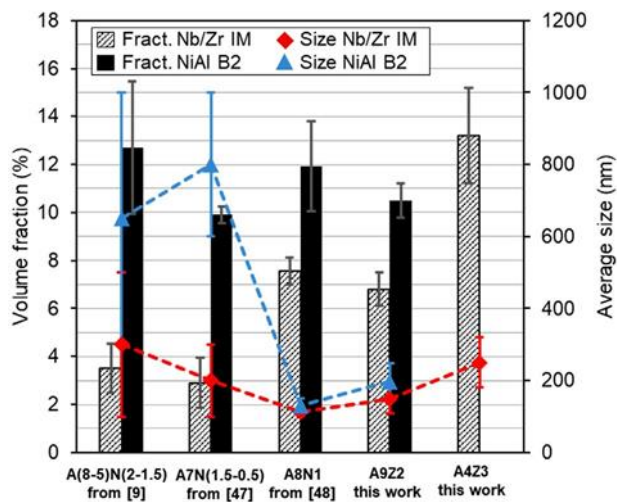

Fig. 11. Average volume fraction and size of A9Z2 and A4Z3 compared to Typical AFA Steels with compositional ranges A(8-5)N(2-0.5). A denotes the Al content, N the Nb content and Z the Zr content in at.% respectively. Error bars represent the standard deviation of the calculated average values.

Phase identification and analysis

The analysis through HEXRD (Fig. 3) revealed 4 clear FCC peaks belonging to the matrix, as well as peaks of medium and low intensity peaks corresponding to Zr-rich IM phases and 3 BCC peaks attributed to the NiAl B2 phase. Since A4Z3 did not show any presence of NiAl B2 (Fig. 1d), the scarce and low intensity BCC peaks for this HEA are most likely remnant traces of unmolten Cr from the *in-situ* alloying. Such local segregations and minor heterogeneities are known to appear *in-situ* alloying in LPBF but can be overcome by adjusting powder feedstock or process parameters [36,50,51]. Moreover, local chemical differences may lead to phase variations. This is especially prone for Fe and Ni combined with Zr, where multiple stable IM phases can be formed depending on the range of M (*M*=Fe,Mo,Co) to Zr ratios [19,52]. The presence of multiple Zr-rich phases is also visualized through the difference in contrast and brightness in the SEM images (Fig. 1d and h).

It is remarkable that the main Zr-rich IM phase in the presented HEAs was the cubic $M_{23}Zr_6$ type and not the cubic M_2Zr C15 type Laves phase. In the case of AFA steels with Nb, instead of Zr, the formed Laves phase is the hexagonal Fe_2Nb C14 [53]. For Fe-Cr-Zr alloys, the hexagonal structure is also the present one, where Cr stabilizes the C14 and C36 structure, but increasing Ni content stabilizes the cubic Fe_2Zr C15 Laves [23,19]. This has also been reported for CoCrFeNiZr$_X$ HEAs, which typically present the M_2Zr C15 Laves, and depending on the Zr content, also traces of the monoclinic Ni_7Zr_2 phase [18,25,54]. Since for binary systems of Fe-Zr and Co-Zr the M_2Zr type is the more stable IM compared to $M_{23}Zr_6$ or M_5Zr, the 2:1 ratio of M to Zr was the expected one for the here presented HEAs [55–57].

In the case of the Ni-Zr system high cooling rates can suppress the primary Ni_7Zr_2 phase and allow the peritectic phase Ni_5Zr, with slight lower Zr content, to solidify directly form the melt [58]. Furthermore, all three binary phase diagrams Fe-Zr, Ni-Zr and Co-Zr have a similar arrangement of invariant reactions for the lower Zr contents. Considering this same

arrangement, it is fair to assume that this effect also applies for Fe-Zr and Co-Zr, where the high cooling rates suppress the primary M_2Zr and the peritectic M_{23}Zr$_6$ is formed. The phenomenon of high cooling rates promoting the 23:6 over the 2:1 ratio was also reported by Ohodnicki et al. [57] for metallic glasses of $(FeCoNi)_2$Zr composition.

Like these metallic glasses, the presented HEAs also are constituted of elements with dissimilar sizes such as the larger Zr, and smaller Al compared to Co, Cr, Fe or Ni [18,57]. Given this size misfit in the HEAs and the high cooling rates of LPBF, the 23:6 stabilization over the 2:1 ratio seems plausible.

Alike AFA steels, only one type of Fe-Zr IM phase was expected. However, Chen et al. [19] reported the coexistence of multiple IM phases in Fe-rich Fe-Cr-Ni-Zr alloys, similar to the here presented HEAs. Furthermore, Chen et al. [19] showed a high solubility of Ni in the Fe_{23}Zr$_6$ phase and reported that the three phases BCC, Fe_2Zr C15 and Fe_{23}Zr$_6$ stably coexist for a variety of compositions and temperatures. Additionally, the Ni_7Zr$_2$ phase would appear for those compositions with sufficient Ni content [19]. Taking this into account, combined with the out-of-equilibrium solidification, and the additional presence of Co and Al in the Fe-rich HEAs of this work, the coexistence of the multiple phases is reasonable.

In the diffractograms of Fig. 3 the presence of multiple phases in different fractions led to partial and full overlaps on the 2θ positions. In particular, the high intensity peaks of the FCC and BCC phase overlay multiple reflexes of the Zr-rich IM phases. This hinders a clear identification of all phases through Rietveld refinement. The highest intensity peak of the M_{23}Zr$_6$ phase corresponds to {511} at a 2θ of ~3.2° (usage of approximated values to cover the variation between A4Z3, A9Z3 and the different temperatures). Despite their low intensity, the other marked M_{23}Zr$_6$ peaks were unambiguously identified by HERXD. All peaks marked as M_xZr$_y$ in Fig. 3 could not be identified because of the potential overlaps. This issue is mainly attributed to the presence of Ni_7Zr$_2$, which due to

its Monoclinic crystal structure has low symmetry and therefore a large number of potential reflexes [59]. The small peak at ~2.4° would fit for the monoclinic Ni_7Zr_2 and the cubic Ni_5Zr. The right shoulder of the double peak at ~3.0 could belong either to Ni_7Zr_2 or to M_2Zr. And the peaks at ~2.5°, ~4.35°, ~4.7°, ~5.3°, and ~6.2° would fit equally for Ni_7Zr_2 and $M_{23}Zr_6$. But also, the cubic phases overlap in some positions, like Ni_5Zr with $M_{23}Zr_6$ at ~4.3° and ~5.6° or M_2Zr with $M_{23}Zr_6$ at ~6.3° Unfortunately, due to the small precipitate size and sample preparation limitations, EDS and EBSD analysis were not able to contribute for further phase clarification. For this reason, all further analysis was limited to the identified FCC matrix, the BCC NiAl B2 and $M_{23}Zr_6$ IM precipitates. Future work should consider prealloyed powder feedstocks to avoid local chemical variations and use transmission electron microscopy selected area diffraction to improve phase identification. The identified lattice parameters, as well as the CTEs and their evolution over the temperature in an uncompressed state are displayed in Fig. 4. The RT lattice parameters for the FCC matrix with 3.64 Å and 3.66 Å, for A4Z3 and A9Z2 respectively, are slightly larger than in typical AFA steels (~3.60 Å). Also, the BCC NiAl B2 of A9Z2 with 2.94 Å, has a small increase compared to conventional AFA candidates (~2.89 Å) [53,60]. The increase of lattice parameter due to lattice distortion resulting from the multi-element mixture is a known effect for HEAs [15,24]. Since the compositional ranges were close to highly alloyed AFA steels, this effect appears weak on the FCC matrix and BCC precipitates but

is much more pronounced for the $M_{23}Zr_6$ phase when compared to a single metal type. With M being compositionally fixed for Fe, Ni, or Co, the lattice parameters would be 11.58 Å, 11.49 Å, and 11.43 Å respectively, but in the multielement mixture of A4Z3 and A9Z2 the lattice parameters for $M_{23}Zr_6$ were 11.79 Å and 11.85 Å respectively [56,57]. A9Z2 showed larger lattice parameters than A4Z3 for the same phase type. Typically, the lattice parameter would increase with higher Zrcontent, but a larger amount of solute Al could decrease the

lattice parameter by adding further distortion [24]. Since in A9Z2 the NiAl B2 phase takes the major Al content, it seems reasonable that the amount of solute Al in FCC matrix and $M_{23}Zr_6$ would be larger for A4Z3. With rising temperature, the lattices expand, and the lattice parameter differences between A4Z3 and A9Z2 become smaller (left side of Fig. 4). This is further visible in the CTE values, which are overall larger for A4Z3 than A9Z2 (right side of Fig. 4). This aligns well with the larger amount of solute Al together with the higher Zr content and could be further augmented by the increased Co content in A4Z3. Matsura et al. [61] reported that the addition of Co and Fe into NiAl alloys would notably increase the CTE. This effect would be more pronounced for higher Co

fractions.

Compression behavior and lattice strain analysis

As visible in the compressive stress-strain curves from Fig. 5 and the yield stress values in Table 3, the A9Z2 alloy has a higher strength than A4Z3 throughout all temperatures. This is mainly attributed to the presence of NiAl B2 precipitates in A9Z2. The overall volume fraction of precipitates ($M_{23}Zr_6$ + NiAl B2) for A9Z2 is larger than for A4Z3 (Fig. 11) and the finer particle size and distribution also led to smaller inter-particle distances δ (Table 2) which increased the alloys strength.

The contribution of the NiAl B2 is also visible in the change of hardness from the as-built to the heat-treated state. The as-built microstructures of both HEAs (Fig. 1(a), (b), (e) and (f)) showed the same hardness. Both alloys presented the cellular structure with the Zr rich phases and were subjected to residual stress from the rapid solidification which adds further strength. Through the heat treatment, the stress is relieved for both alloys, relaxing the matrix and homogenizing the precipitates distribution, but the precipitation of NiAl B2 compensates the drop in hardness for A9Z2.

The compressive yield strength at RT of 630 MPa for A4Z3 and 780 MPa for A9Z2 is

outperforming other Al containing precipitation hardened austenitic HEAs, ranging from 400 to 600 MPa [62,63]. Also, for conventional manufactured HEAs, the achieved strength through precipitation hardening is dependent on the size fraction and distribution of the precipitates. According to the work of Ma et al. [62], HEAs from the Al-Co-CrFe-Ni system composed of an FCC matrix and ∼15% volume fraction of NiAl B2 precipitates would present differences from compressive to tensile yield strength of around 40 MPa. Considering this, A4Z3 and A9Z2, can be assumed as comparable to AFA steels which typically range from 300 to 800 MPa tensile strength at RT, depending on composition and treatment condition [9]. Highly thermomechanically processed HEAs of similar composition have reported yield strength of 860 MPa [14] and some AFA steels ≥1000 MPa [12]. AFA steels achieve this high yields at RT due to grain refinement but this strengthening effect drops drastically between 600 °C and 700 °C, from where softened grain boundaries act as weak points [12,48]. This drop is less pronounced for precipitation hardened Al containing austenitic HEAs [14,63]. Consistently, the alloys investigated in this study showed a gentle reduction in yield strength with rising temperature. At 800 °C A4Z3 and A9Z2 presented compressive yields of 230 MPa and 260 MPa respectively. This confirms the large and elongated grains with high fractions of IM precipitates as a suitable high-temperature resistant microstructure. Additionally, it should be mentioned that the slow strain rate of 0.001 s^{-1} was applied for the sake of the *in-situ* HEXRD analysis, but at high temperatures the yield of AFA steels or Al containing austenitic HEAs is strongly strain rate dependent [12,63–65]. This suggests that higher yield strengths for A4Z3 and A9Z2 would be achieved if examined at more moderate strain rates. Nevertheless, the discrepancy of compression to tensile yield for the presented HEAs should be investigated in future studies.

The waterfall plot in Fig. 6 depicts the diffractograms of A9Z2 along the deformation at RT. The enlarged sections (Fig. 6 (a–c) visualize examples of lattice strain induced peak shift, intensity drop, broadening and features responsible for some of the misfits of the statistical

model. In the selection of reflexes for lattice strain and FWHM for both alloys and throughout the temperatures (Figs. 7–9), some curves present anomalous sections or outlying behavior resulting from the model misfits. Since the concurrent display of axial and radial integration can compensate for some of the outliers, these curves were kept for completeness, but were not treated in this discussion. A potential explanation for some misfit producing features like shown in Fig. 6(b) could be the formation of cracks or stacking faults which are known to produce small discontinuities [66], but an accurate examination of this features is beyond the scope of this work.

In the lattice strain plots, the presence of NiAl B2 (BCC) is the main difference between A4Z3 and A9Z2 (Fig. 7(a) and (b)). The relatively large amount of lattice strain corresponding to the BCC {200} reflex indicates the load induced deformation and therefore its strength contribution to the material. Additionally, due to the higher stress reached in A9Z2 compared to A4Z3, the lattice strain values of the FCC and $M_{23}Zr_6$ reflexes of A9Z2 were slightly larger than for A4Z3. Fig. 7(a) and (b) also depict how the IMs $M_{23}Zr_6$ and NiAl B2 develop larger lattice strain values along the RT compression as compared to the FCC matrix. Generally, different phases and the differently oriented reflections have different elastic modulus and are therefore harder or easier to deform, resulting in different lattice strain and strength contribution. This is clearly visible for both alloys by the differences in axial lattice strain (ε) of the FCC peaks with values being $\varepsilon\{200\} > \varepsilon\{311\} > \varepsilon\{220\}$ consistent with the elastic modulus (E) of the orientations $E\{220\} > E\{311\} > E\{200\}$, resulting from the planar density. Furthermore, the direction of load (tension/compression) and the texture of the material have a strong influence on different impact of phases and orientations, accounting for the main differences of lattice strain between the axial and radial integration [35,67,68].

The differences of axial and radial integration, and between different phases and their orientations are also reflected in the stress induced peak broadening, quantified by the evolution of the FWHM. The FWHM values at RT and throughout the temperatures are overall larger for

A9Z2 than for A4Z3 (Figs. 7 (c–f) and 9). It is also visible how the reflexes of the relatively soft FCC phase show a larger increase in FWHM than the ones belonging to the harder $M_{23}Zr_6$ phase. The FCC reflexes show a noticeable large FWHM and partially unsteady increase for A9Z2, irrespective of axial or radial integration. With A9Z2 being subjected to higher stresses than A4Z3, the increased FWHM could be explained by larger microstrains arising from the formation of dislocations. However, it should be considered that peak broadening can arise not only from stress induced dislocations but also from high temperature expansion, or other changes and defects to the initial crystal arrangement [69].

The decrease of lattice strain and FWHM with increasing temperature (Figs. 8 and 9) goes along with the temperature related stress reduction. The difference in yield strength between A4Z3 and A9Z2 becomes smaller with increasing temperature. This is due to the softening of the BCC phase, reducing its strength contribution. The ordered NiAl B2 phase is known to appear as a compound with certain solubility for other elements e.g. Cr or Co [61,70]. It's been reported that depending on the AFA steel composition, the NiAl B2 compound displays a brittleductile transition between 500 and 800 °C and is considered as ineffective for strength contribution at higher temperatures [71]. For the A9Z2 HEA, the NiAl B2 softening is visible as a relaxation in the lattice strain of the {200} BCC reflex starting from 700 °C (Fig. 8(e)). Nevertheless, at 900 °C the reduced but still considerable values of lattice strain and FWHM suggest that the NiAl B2 precipitates keep contributing to the strength of A9Z2 at high temperatures. Given the neglectable difference in yield strength at 900 °C between A9Z2 and A4Z3, it is fair to assume that the FCC matrix of A4Z3 with an increased content of Co and Zr has slightly better high temperature resistance. An additional indication for this is the greater strain hardening of A4Z3 visible in the slope difference of the stress-strain curves from 700 °C-900 °C (Fig. 5). The {222} reflex as representative of the $M_{23}Zr_6$ phase also shows a slight relaxation as reduction of lattice strain during the ongoing compression for both alloys at 700 °C and 800 °C. However, the low lattice strain values at higher temperatures as well

as the small FWHM throughout all temperatures indicate a high stiffness of the IM phase. This is affirmed by the work of Du et al. [56] reporting that for Ni the $M_{23}Zr_6$ type IM is, besides M_5Zr, the one with the largest shear and elastic modulus of the M_xZr_y IMs.

The FCC matrix takes the lowest lattice strain at RT but shows the smallest reduction with increasing temperature and no relaxation with ongoing compression. A consistent decrease is visible in the evolution of the FWHM for the representative {200} FCC reflex. This homogenous lattice deformation is also visible in the unaltered texture throughout the compression and temperatures (Fig. 10). As in the EBSD result from Fig. 2, the matrix texture analysis through the E-WIMV algorithm in Fig. 10 shows the cubic texture aligned with the build direction. For both alloys, no indications of phase transformations or recrystallisation appeared during the high temperature compression. At 20% strain, A4Z3 appears to have a slightly stronger blurring of the initial texture at 700 °C and 900 °C than A9Z2. This is most likely related to the compositional based differences accounting for the discrepancy in strain hardening and load pick-up through IM phases as previously described.

Generally, the softening of matrix and IM phases is expected for high temperatures. The typical Fe_2Nb Laves phase in AFA steels is known to present softening for ≥700 °C and still contribute to the overall strength [66]. The same applies for the NiAl B2 precipitates, which despite brittle-ductile transition still increase the resistance to creep deformation in AFA steels. Above 700 °C, fine dispersed precipitates within grains, typically carbides, are the effective strengthening mechanism for AFA steels [9]. With the absence of carbides, the presented HEAs relay on the distribution of nm-sized $M_{23}Zr_6$ and NiAl B2, but also the small fractions of unidentified M_xZr_y. These could not be considered in the lattice strain and FWHM analysis but are expected to contribute to the materials strength. Considering this and the large, elongated grains of the LPBF approach, it is fair to assume that both presented HEAs have an acceptable high temperature creep resistance. A9Z2 would be expected to perform slightly better than A4Z3, but requires further investigation. The overall high

temperature compression performance of the alloys and their microstructural comparison to related HEA and AFA steels, showed the potential of this LPBF approach. Future work should consider further compositional adjustments and an assessment of tensile and creep properties.

Summary and conclusions

Two HEAs of the Al-Co-Cr-Fe-Ni-Zr system have been investigated using LPBF manufacturing to investigate new austenitic materials for high temperature applications. The two HEAs, (A4Z3) and (A9Z2), have a cost-effective Fe-rich baseline and compositional similarities to AFA steels. The alloys have been prepared with distinct Al and Zr content, as to obtain distinct IM phases and evaluate their contribution to the strengthening. For a more comprehensive analysis of the high temperature behavior and strength contribution of the different phases, the alloys were subjected to *in-situ* synchrotron HEXRD compression tests from RT to 900 °C. The main findings can be summarized as follows:

- Both HEAs presented typical LPBF cellular/dendritic microstructure in the as-built state. Stress relief and aging was performed in a single heat treatment (950 °C / 6 h). The achieved microstructures were composed of large, elongated grains containing multiple types of finely dispersed nano-sized IM phases.

- The achieved refinement and dispersion of IMs inside the FCC matrix through LPBF are comparable to the capabilities of conventional multi-thermo-mechanical treatments in similar HEAs or AFA steels.

- The main Zr rich IM phase for both alloys was the $M_{23}Zr_6$ type, stabilized by the HEA composition and the high cooling rates of the LPBF process.

- The multielement HEA approach let to a strong increase in lattice parameter for the $M_{23}Zr_6$ IM phase as compared to simple binary Fe-, Ni or Co-Zr candidates.

- The increase of Zr content from 2 to 3 at.% led to an increased fraction, size and interparticle

spacing of the Zr-rich precipitates.

- The Al content of 4 at% was below the solubility limit of the FCC HEA matrix. The Al content of 9 at.% led to a volume fraction of 10% NiAl B2 precipitates.

- The presence of NiAl B2 adds further strength to A9Z2 but the effect is diminished above 700 °C. This is due to the phase softening as visible from the relaxation in the lattice strain evolution during compression.

- The achieved compressive RT yield strengths were 630 MPa and 780 MPa for A4Z3 and A9Z2, respectively. Both alloys presented a continuous moderate drop in strength with increasing temperature.

- No changes in texture or phase transformations were detected for the FCC matrix of both HEAs during the compression tests from RT up to 900 °C. This is affirmed by the homogenous decrease of lattice strain and FWHM with rising temperature.

The presented LPBF approach produced microstructures of similar morphology and refinement to conventionally thermo-mechanical processing. The achieved RT and high temperature yield strength was also comparable to conventionally manufactured AFA steels or related Al containing austenitic HEAs. For a more complete assessment, tensile properties, creep, and oxidation resistance of the presented HEAs should be investigated in future work. Nevertheless, the achieved material performance, in combination with the design freedom of the LPBF process, showed the great potential of Fe-rich austenitic materials for heatresistant structural components and a possible alternative to Ni-based alloys.

Acknowledgements

References

[1] Y. Yamamoto, M.P. Brady, Z.P. Lu, C.T. Liu, M. Takeyama, P.J. Maziasz, B.A. Pint, Alumina-forming austenitic stainless steels strengthened by laves phase and MC carbide precipitates, Metall. Mater. Trans. A Phys. Metall. Mater. Sci. 38 A (2007) 2737– 2746, doi:10.1007/s11661-007-9319-y.

[2] J. Choi, C.S. Seok, S. Park, G. Kim, Effect of higherature degradation on microstructure evolution and mechanical properties of austenitic heat-resistant steel, J. Mater. Res. Technol. 8 (2019) 2011–2020, doi:10.1016/j.jmrt.2018.11.017.

[3] S.W. Chen, C. Zhang, Z.X. Xia, H. Ishikawa, Z.G. Yang, Precipitation behavior of Fe_2 Nb Laves phase on grain boundaries in austenitic heat resistant steels, Mater. Sci. Eng. A 616 (2014) 183–188, doi:10.1016/j.msea.2014.07.104.

[4] Y.H. Zhang, M. Li, L.A. Godlewski, J.W. Zindel, Q. Feng, Effective design of new austenitic cast steels for ultra-high temperature automotive exhaust components through combined CALPHAD and experimental approaches, Mater. Sci. Eng. A 683 (2017) 195–206, doi:10.1016/j.msea.2016.12.023.

[5] P.J. Maziasz, Development of creep-resistant and oxidation-resistant austenitic stainless steels for high temperature applications, JOM 70 (2018) 66–75, doi:10.1007/s11837-017-2642-x.

[6] T. Jozaghi, C. Wang, R. Arroyave, I. Karaman, Design of alumina-forming austenitic stainless steel using genetic algorithms, Mater. Des. 186 (2020), doi:10.1016/j.matdes.2019.108198.

[7] M. Takeyama, Novel concept of austenitic heat resistant steels strengthened by intermetallics, Mater. Sci. Forum 539-543 (2007) 3012–3017, doi:10.4028/www.scientific.net/msf.539-543.3012.

[8] Y. Yamamoto, M. Takeyama, Z.P. Lu, C.T. Liu, N.D. Evans, P.J. Maziasz, M.P. Brady, Alloying effects on creep and oxidation resistance of austenitic stainless steel alloys employing intermetallic precipitates, Intermetallics 16 (2008) 453–462 (Barking), doi:10.1016/j.intermet.2007.12.005.

[9] Y. Yamamoto, M.P. Brady, M.L. Santella, H. Bei, P.J. Maziasz, B.A. Pint, Overview of strategies for high-temperature creep and oxidation resistance of alumina-forming austenitic stainless steels, Metall. Mater. Trans. A Phys. Metall. Mater. Sci. 42 (2011) 922–931, doi:10.1007/s11661-010-0295-2.

[10] I. Tarigan, N. Takata, M. Takeyama, Grain Boundary Precipitation Strengthening Mechanism By Fe 2 Nb Laves Phase in Creep of Fe-20Cr-30Ni-2Nb Austenitic Heat Resistant Steel, Creep and Fracture of Engineering Materials and Structures, Japan Institute of Metals, 2012.

[11] M.P. Brady, J. Magee, Y. Yamamoto, D. Helmick, L. Wang, Co-optimization of wrought alumina-forming austenitic stainless steel composition ranges for hightemperature creep and oxidation/corrosion resistance, Mater. Sci. Eng. A 590 (2014) 101–115, doi:10.1016/j.msea.2013.10.014.

[12] B. Hu, I. Baker, The effect of thermo-mechanical treatment on the high temperature tensile behavior of an alumina-forming austenitic steel, Mater. Sci. Eng. A 651 (2016) 795–804, doi:10.1016/j.msea.2015.11.036.

[13] I. Baker, N. Afonina, Z. Wang, M. Wu, Preliminary creep testing of the aluminaforming austenitic stainless steel Fe-20Cr-30Ni-2Nb-5Al, Mater. Sci. Eng. A Struct. Mater. 718 (2018) 492–498, doi:10.1016/j.msea.2018.01.090.

[14] Z. Li, L. Fu, J. Peng, H. Zheng, X. Ji, Y. Sun, S. Ma, A. Shan, Improving mechanical properties of an FCC high-entropy alloy by γ' and B2 precipitates strengthening, Mater. Charact. 159 (2020) 109989, doi:10.1016/j.matchar.2019.109989.

[15] B.S. Murty, J.W. Yeh, S. Ranganathan, High entropy alloys, 2014. 10.1016/B978-012-800251-3.00010-9.

[16] D.B. Miracle, O.N. Senkov, A critical review of high entropy alloys and related concepts, Acta Mater. 122 (2017) 448–511, doi:10.1016/j.actamat.2016.08.081.

[17] H. Jiang, K. Han, X. Gao, Y. Lu, Z. Cao, M.C. Gao, J.A. Hawk, T. Li, A new strategy to design eutectic high-entropy alloys using simple mixture method, Mater. Des. 142 (2018) 101–105, doi:10.1016/j.matdes.2018.01.025.

[18] S. Sheikh, H. Mao, S. Guo, Predicting solid solubility in CoCrFeNiMx (M = 4d transition metal) high-entropy alloys, J. Appl. Phys. 121 (2017) 1–8, doi:10.1063/1.4983762.

[19] T. Chen, Y. Yang, L. Tan, Phase stability in the Fe-Rich Fe-Cr-Ni-Zr alloys, Metall. Mater. Trans. A Phys. Metall. Mater. Sci. 48 (2017) 5009–5016, doi:10.1007/s11661-017-4253-0.

[20] C.S. Tiwary, A. Kashiwar, S. Bhowmick, K.C. Hari Kumar, K. Chattopadhyay, D. Banerjee, Engineering an ultrafine intermetallic eutectic ternary alloy for high strength and high temperature applications, Scr. Mater. 157 (2018) 67–71, doi:10.1016/j.scriptamat.2018.07.036.

[21] C. Tiwary, V.V. Gunjal, D. Banerjee, K. Chattopadhyay, Intermetallic eutectic alloys in the Ni-Al-Zr system with attractive high temperature properties, MATEC Web Conf. 14 (2014) 01005, doi:10.1016/j.biopsycho.2011.09.001.

[22] P. Donnadieu, C. Pohlmann, S. Scudino, J.J. Blandin, K. Babu Surreddi, J. Eckert, Deformation at ambient and high temperature of *in situ* Laves phases-ferrite composites, Sci. Technol. Adv. Mater. 15 (2014), doi:10.1088/1468-6996/15/3/034801.

[23] L. Tan, Y. Yang, Microstructure and Mechanical Properties of Laves Phasestrengthened Fe-Cr-Zr Alloys, Metall. Mater. Trans. A Phys. Metall. Mater. Sci.

46 (2015) 1188–1195, doi:10.1007/s11661-014-2695-1.

[24]   W. Huo, H. Zhou, F. Fang, Z. Xie, J. Jiang, Microstructure and mechanical properties of CoCrFeNiZr x eutectic high-entropy alloys, Mater. Des. 134 (2017) 226–233, doi:10.1016/j.matdes.2017.08.030.

[25]   R. Jain, A. Jain, M.R. Rahul, A. Kumar, M. Dubey, R.K. Sabat, S. Samal, G. Phanikumar, Development of ultrahigh strength novel Co–Cr–Fe–Ni–Zr quasi-peritectic high entropy alloy by an integrated approach using experiment and simulation, Materialia 14 (2020) (Oxf), doi:10.1016/j.mtla.2020.100896.

[26]   G.B. Shan, Y.Z. Chen, Y.J. Li, C.Y. Zhang, H. Dong, Y.B. Cong, W.X. Zhang, L.K. Huang, T. Suo, F. Liu, High temperature creep resistance of a thermally stable nanocrystalline Fe-5 at.% Zr steel, Scr. Mater. 179 (2020) 1–5, doi:10.1016/j.scriptamat.2019.12.036.

[27]   T.G. Langdon, An analysis of flow mechanisms in high temperature creep and superplasticity, Mater. Trans. 46 (2005) 1951–1956, doi:10.2320/matertrans.46.1951.

[28]   T.G. Langdon, Grain boundary sliding revisited: developments in sliding over four decades, J. Mater. Sci. 41 (2006) 597–609, doi:10.1007/s10853-006-6476-0.

[29]   T. Debroy, H.L. Wei, J.S. Zuback, T. Mukherjee, J.W. Elmer, J.O. Milewski, A.M. Beese, A. Wilson-heid, A. De, W. Zhang, Additive manufacturing of metallic components – process, structure and properties, Prog. Mater. Sci. 92 (2018) 112– 224, doi:10.1016/j.pmatsci.2017.10.001.

[30]   G. Boussinot, M. Apel, J. Zielinski, U. Hecht, J.H. Schleifenbaum, Strongly out-ofequilibrium columnar solidification during laser powder-bed fusion in additive manufacturing, Phys. Rev. Appl. 11 (2019) 1, doi:10.1103/PhysRevApplied.11.014025.

[31]   P. Bajaj, A. Hariharan, A. Kini, P. Kürnsteiner, D. Raabe, E.A. Jägle, Steels in additive manufacturing: a review of their microstructure and properties, Mater. Sci.

Eng. A 772 (2020), doi:10.1016/j.msea.2019.138633.

[32]   S. Ghosh, N. Ofori-Opoku, J.E. Guyer, Simulation and analysis of γ-Ni cellular growth during laser powder deposition of Ni-based superalloys, Comput. Mater. Sci. 144 (2018) 256–264, doi:10.1016/j.commatsci.2017.12.037.

[33] P. Staron, T. Fischer, T. Lippmann, A. Stark, S. Daneshpour, D. Schnubel, E. Uhlmann, R. Gerstenberger, B. Camin, W. Reimers, E. Eidenberger, H. Clemens, N. Huber, A. Schreyer, *In situ* experiments with synchrotron high-energy X-rays and neutrons, Adv. Eng. Mater. 13 (2011) 658–663, doi:10.1002/adem.201000297.

[34]   P. Erdely, T. Schmoelzer, E. Schwaighofer, H. Clemens, P. Staron, A. Stark, K.D. Liss, S. Mayer, *In situ* characterization techniques based on synchrotron radiation and neutrons applied for the development of an engineering intermetallic titanium aluminide alloy, Metals 6 (2016) 1–27 (Basel), doi:10.3390/met6010010.

[35]   N. Xu, S. Li, R. Li, M. Zhang, Z. Yan, Y. Cao, Z. Nie, Y. Ren, Y.D. Wang, *In situ* investigation of the deformation behaviors of Fe20Co30Cr25Ni25 and Fe20Co30Cr30Ni20 high entropy alloys by high-energy X-ray diffraction, Mater. Sci. Eng. A 795 (2020) 1–19, doi:10.1016/j.msea.2020.139936.

[36]   M.S. Knieps, W.J. Reynolds, J. Dejaune, A.T. Clare, A. Evirgen, *In-situ* alloying in powder bed fusion : the role of powder morphology, Mater. Sci. Eng. A 807 (2021) 1–12, doi:10.1016/j.msea.2021.140849.

[37]   B. Delaunay, Sur la sphere vide. A la memoire de Georges Voronoi, Bulletin de l'Academie Des Sciences de l'URSS. Classe Des Sciences Mathematiques et Naturelles. (1934) 793–800.

[38]   Y. Estrin, J. Lepinoux, Heterogeneously distributed particles : modelling, Acta Mater. 48 (2000) 4337–4347.

[39]   C.A. Schneider, W.S. Rasband, K.W. Eliceiri, NIH Image to ImageJ: 25 years of image analysis, Nat. Methods 9 (2012) 671–675, doi:10.1038/nmeth.2089.

[40]   N. Schell, A. King, F. Beckmann, T. Fischer, M. Müller, A. Schreyer, The high energy materials science beamline (HEMS) at PETRA III, Mater. Sci. Forum 772 (2014) 57– 61, doi:10.4028/www.scientific.net/MSF.772.57.

[41]   P. Barriobero-Vila, J. Gussone, K. Kelm, J. Haubrich, A. Stark, N. Schell, G. Requena, An *in situ* investigation of the deformation mechanisms in a *β*quenched Ti-5Al-5V-5Mo-3Cr alloy, Mater. Sci. Eng. A 717 (2018) 134–143, doi:10.1016/j.msea.2018.01.077.

[42]   L. Lutterotti, S. Matthies, H.R. Wenk, A.S. Schultz, J.W. Richardson, Combined texture and structure analysis of deformed limestone from time-of-flight neutron diffraction spectra, J. Appl. Phys. 81 (1997) 594–600, doi:10.1063/1.364220.

[43]   Y. Zoo, D. Adams, J.W. Mayer, T.L. Alford, Investigation of coefficient of thermal expansion of silver thin film on different substrates using X-ray diffraction, Thin Solid Films 513 (2006) 170–174, doi:10.1016/j.tsf.2006.02.005.

[44]   A. Dutta, D. Barman, J. Das, Strengthening ultrafine lamellar Ni-Zr-(Al) eutectic by precipitation hardening, J. Alloy. Compd. 882 (2021) 160684, doi:10.1016/j.jallcom.2021.160684.

[45]   Y. Ma, B. Jiang, C. Li, Q. Wang, C. Dong, P.K. Liaw, F. Xu, L. Sun, The BCC/B2 morphologies in Al x NiCoFeCr high-entropy alloys, Metals 7 (2017) (Basel), doi:10.3390/met7020057.

[46]   Y. Yamamoto, M.P. Brady, G. Muralidharan, B.A. Pint, P.J. Maziasz, D. Shin, B. Shassere, S.S. Babu, C.H. Kuo, Development of creep-resistant, alumina-forming ferrous alloys for high-temperature structural use, in: Proceedings of the ASME Symposium on Elevated Temperature Application of Materials for Fossil, Nuclear, and Petrochemical Industries ETAM2018, 2018, pp. 1–10.

[47]   F.H. Stott, G.C. Wood, J. Stringer, The influence of alloying elements on the

development and maintenance of protective scales, Oxid. Met. 44 (1995) 113–145, doi:10.1007/BF01046725.

[48] Q. Gao, C. Jiang, H. Zhang, Q. Ma, H. Zhang, Z. Liu, H. Li, Co-strengthening of dislocations and precipitates in alumina-forming austenitic steel with cold rolling followed by aging, Mater. Sci. Eng. A 831 (2022) 142181, doi:10.1016/j.msea.2021.142181.

[49] N.G. Jones, R. Izzo, P.M. Mignanelli, K.A. Christo, H.J. Stone, Intermetallics phase evolution in an Al 0 . 5 CrFeCoNiCu high entropy alloy, 71 (2016) 43–50. 10.1016/j.intermet.2015.12.001.

[50] S. Ewald, F. Kies, S. Hermsen, M. Voshage, C. Haase, J.H. Schleifenbaum, Rapid alloy development of extremely high-alloyed metals using powder blends in laser powder bed fusion, Materials 12 (2019) 1–15 (Basel), doi:10.3390/MA12101706.

[51] L.S. Aota, P. Bajaj, H.R.Z. Sandim, E.A. Jägle, Laser powder-bed fusion as an alloy development tool : parameter selection for *in-situ* alloying using elemental powders, Materials 13 (18) (2020) 1–17, doi:10.3390/ma13183922.

[52] Z. Du, L. Zou, C. Ping Guo, X. Ping Ren, C. Rong Li, Phase stability of Fe23Zr6 and thermodynamic reassessment of Fe–Zr system, J. Iron Steel Res. Int. 28 (2021) 1375–1389, doi:10.1007/s42243-021-00570-w.

[53] G. Trotter, B. Hu, A.Y. Sun, R. Harder, M.K. Miller, L. Yao, I. Baker, Precipitation kinetics during aging of an alumina-forming austenitic stainless steel, Mater. Sci. Eng. A 667 (2016) 147–155, doi:10.1016/j.msea.2016.04.081.

[54] S. Vrtnik, S. Guo, S. Sheikh, A. Jelen, P. Koželj, J. Luzar, A. Kocjan, Z. Jagličić, A. Meden, H. Guim, H.J. Kim, J. Dolinšek, Magnetism of CoCrFeNiZrxeutectic high-entropy alloys, Intermetallics 93 (2018) 122–133 (Barking), doi:10.1016/j.intermet.2017.11.017.

[55] H.J. Lu, N. Zou, X.S. Zhao, J.Y. Shen, X.G. Lu, Y.L. He, Thermodynamic

investigation of the Zr-Fe-Nb system and its applications, Intermetallics 88 (2017) 91–100 (Barking), doi:10.1016/j.intermet.2017.05.008.

[56]   J. Du, B. Wen, R. Melnik, Y. Kawazoe, First-principles studies on structural, mechanical, thermodynamic and electronic properties of Ni-Zr intermetallic compounds, Intermetallics 54 (2014) 110–119 (Barking), doi:10.1016/j.intermet. 2014.05.021.

[57]   P.R. Ohodnicki, N.C. Cates, D.E. Laughlin, M.E. McHenry, M. Widom, Ab initio theoretical study of magnetization and phase stability of the (Fe,Co,Ni)23B6 and (Fe,Co,Ni)23Zr6 structures of Cr23C6 and Mn23Th6 prototypes, Phys. Rev. B Condens. Matter Mater. Phys. 78 (2008) 1–13, doi:10.1103/PhysRevB.78.144414.

[58]   Y.F. Si, H.P. Wang, P. Lü, B. Wei, Peritectic solidification mechanism and accompanying microhardness enhancement of rapidly quenched Ni–Zr alloys, Appl. Phys. A Mater. Sci. Process. 125 (2019) 1–13, doi:10.1007/s00339-019-2399-x.

[59]   R.E. Dinnebier, S.J.L. Billinge, Chapter 1 "Principles of Powder Diffraction", in: Powder Diffraction: Powder Diffraction: Theory and Practice, RSC, 2008, pp. 1–19. ISBN: 978-0-85404-231-9.

[60]   Z.C.B. Hu, G. Trotter, I. Baker, M.K. Miller, L. Yao, S. Chen, The effects of cold work on the microstructure and mechanical properties of intermetallic strengthened alumina-forming austenitic stainless steels, Metall. Mater. Trans. A 8 (2015) 1–22.

[61]   K. Matsuura, T.I. Khan, T. Ohmi, M. Kudoh, Reactive casting of B2-ordered Ni-Al-Co ternary intermetallic alloys, Mater. Trans. 42 (2001) 263–268, doi:10.2320/matertrans.42.263.

[62]   Y. Ma, Q. Wang, B.B. Jiang, C.L. Li, J.M. Hao, X.N. Li, C. Dong, T.G. Nieh, Con-

trolled formation of coherent cuboidal nanoprecipitates in body-centered cubic highentropy alloys based on Al 2 (Ni,Co,Fe,Cr) 14 compositions, Acta Mater. 147 (2018) 213–225, doi:10.1016/j.actamat.2018.01.050.

[63] C.J. Tong, M.R. Chen, S.K. Chen, J.W. Yeh, T.T. Shun, S.J. Lin, S.Y. Chang, Mechanical performance of the AlxCoCrCuFeNi high-entropy alloy system with multiprincipal elements, Metall. Mater. Trans. A Phys. Metall. Mater. Sci. 36 (2005) 1263–1271, doi:10.1007/s11661-005-0218-9.

[64] Q. Gao, H. Zhang, H. Li, X. Zhang, F. Qu, Y. Jiang, Z. Liu, C. Jiang, Hot deformation of alumina-forming austenitic steel: EBSD study and flow behavior, J. Mater. Sci. 54 (2019) 8760–8777, doi:10.1007/s10853-019-03513-9.

[65] R. Luo, Q. Zheng, J.J. Zhu, S. Guo, D.S. Li, G.F. Xu, X.N. Cheng, Dynamic recrystallization behavior of Fe–20Cr–30Ni–0.6Nb–2Al–Mo alloy, Rare Met. 38 (2019) 181– 188, doi:10.1007/s12598-016-0871-8.

[66] B. Hu, I. Baker, High temperature deformation of Laves phase precipitates in alumina-forming austenitic stainless steels, Mater. Lett. 195 (2017) 108–111, doi:10.1016/j.matlet.2017.02.086.

[67] F. Xu, R.A. Holt, E.C. Oliver, M.R. Daymond, Evolution of lattice strains in three dimensions during *in situ* compression of textured Zircaloy-2, J. Neutron Res. 15 (2007) 113–122, doi:10.1080/10238160701372554.

[68] M. Reiberg, X. Li, E. Maawad, E. Werner, Lattice strain during compressive loading of AlCrFeNiTi multi-principal element alloys, Contin. Mech. Thermodyn. (2021), doi:10.1007/s00161-021-00990-9.

[69] L.R. Owen, E.J. Pickering, H.Y. Playford, H.J. Stone, M.G. Tucker, N.G. Jones, An assessment of the lattice strain in the CrMnFeCoNi high-entropy alloy, Acta Mater. 122 (2017) 11–18, doi:10.1016/j.actamat.2016.09.032.

[70] R.W. Cahn, P. Haasen, Physical Metallurgy, 4th ed., Elsevier B.V, 1996.

[71]   H. Bei, Y. Yamamoto, M.P. Brady, M.L. Santella, Aging effects on the mechanical properties of alumina-forming austenitic stainless steels, Mater. Sci. Eng. A 527 (2010) 2079–2086, doi:10.1016/j.msea.2009.11.052.